Optimal dual-PZT sizing and network design for baseline-free SHM of complex anisotropic composite structures

Emmanuel LIZÉ[1], Marc RÉBILLAT[2], Nazih MECHBAL[2] and Christian BOLZMACHER[1]

[1] CEA, LIST, Sensorial and Ambient Interfaces Laboratory, 91191 - Gif-sur-Yvette CEDEX, France.

[2] Processes and Engineering in Mechanics and Materials Laboratory (CNRS, CNAM, ENSAM), 151, Boulevard de l'Hôpital, Paris, F-75013, France.

E-mail: emmanuel.lize@cea.fr

Keywords: Structural Health Monitoring, Lamb Waves, dual PZT, anisotropic composite structure, mode decomposition, baseline free methods.

Abstract

Structural Health Monitoring (SHM) processes for aeronautic composite structures are generally based on the comparison between healthy and unknown databases. The need for prior baseline signals is one of the barriers to an industrial deployment and can be avoided with *"baseline-free"* SHM (BF-SHM) methods based on the attenuations and reflections of symmetric and antisymmetric Lamb waves modes attributable to a damage. A promising mode decomposition method is based on the use of dual PZTs (concentric disc and ring electrodes lying on a single PZT). However, performances of such methods highly depend on the Lamb wave modes properties (propagation speed and attenuation that vary with material orientation and inter-PZT distance), the number and the sensitivity of the dual PZT to each mode (which depends on the frequency and element size). Considering these constraints, an original three-step process able to design a full dual-PZT network and the optimal range of excitation frequencies to consider on a highly anisotropic and arbitrarily complex aeronautic structure is presented. First, the dispersion curves of Lamb waves in the investigated material together with the minimal size

of the damage to detect are used to estimate the size of the dual PZT as well as convenient excitation frequencies. A Local Finite Element Model representative of the full-scale structure is then used to estimate optimal distance and orientation between neighbor PZTs elements. Finally, a network optimization solver applies these parameters to place dual-PZTs on a fan cowl of an aircraft nacelle and provides a candidate network covering the whole structure.

1. Introduction

Monitoring in real-time and autonomously the health state of structures is referred to as Structural Health Monitoring (SHM) [1]. Damage detection using Lamb waves is one of the most common method for the SHM of aeronautic composite structures. Among all the methods employed to trigger and catch Lamb waves, the use of piezoelectric transducer (PZT) is one of the cheapest and easiest-to-settle. The common approach is based on the comparison of signals recorded on a "pristine" structure - the baseline - against those obtained on a possibly damaged structure. The resulting signals that will be used to elaborate damage indexes strongly depend on the structure's mechanical and geometrical properties as well as on environmental conditions. Some solutions have been proposed to compensate for the effect of temperature [2-5] or to extend baseline data to a wider range of environmental conditions [6, 7]. This drawback of existing methods has also fed the interest for "baseline-free" methods. "Baseline-free" is here an abusive word (see Axiom II in [1]) since data, models, or physical assumptions are always needed to decide whether a structure is damaged or not. This expression thus refers here to methods where prior reference signals recorded from the pristine condition of the monitored structure is not necessary for damage detection.

Symmetric and antisymmetric Lamb wave modes are very useful for SHM as they convey complementary information when interacting with damages [8], [9, Ch. 19.4]. Lamb wave modes are related to Lamb solutions for wave propagations in isotropic plates but are also commonly (and abusively) used to designate plate-like waves that propagate in anisotropic materials. Early studies on damage detection in composite structures stated that S_0 mode was more appropriate than A_0 mode for delamination detection since it exhibits higher sensitivity in the structural thickness [8, Para. 3.3]. In

most SHM application on composite structures, S_0 mode is actually preferred since it has lower attenuation, allowing for larger distances between neighbor PZTs in the designed network. However, A_0 mode can be more appropriate since it allows an interaction with a delamination at smaller excitation frequencies than S_0 mode and has been favored in most recent works [10–12]. Actually, both modes can be used as long as the excitation frequency chosen (and the resulting wavelength of each mode) allow an interaction with the damage [9, Para. 19.5.2.2]. Common methods used to study the behavior of a given mode (A_0 or S_0) are based on response signal obtained with collocated transducers [9, Ch. 17], or the use of "sweet spot frequencies" [13, Ch. 8] where only one mode is generated. The former method requires having access to both sides of the instrumented structure and a perfect collocation of the transducers, and the latter restrains the application to specific excitation frequencies that may not correspond to the damage size to detect. Those limitations are overcome by dual PZTs. Dual PZTs are made of a concentric ring and disc as shown in figure 1. Both parts can be used as actuators and sensors bringing more signal combinations than conventional PZTs and allow for the isolation of the first antisymmetric A_0 or symmetric S_0 mode . With dual PZTs, a damage can then be detected in a "*baseline-free*" manner by using the damage-introduced mode conversion and attenuation (which is not the same for each mode) of the propagating waves [8]. The theoretical aspect justifying the use of those PZTs for *"baseline-free"* SHM (BF-SHM) is well developed in [18] and experiments are reported in [19] on aluminum and in [20] on composite structures. However, the interaction of each mode with the damage is conditioned by the wavelength of the waves generated by the dual PZT and the damage dimension. As a consequence, the transducer's dimensions as well as excitation frequencies must be chosen with care. The first objective of the present work is to propose a method for dual-PZT sizing and excitation frequency selection according to the targeted application, *i.e.* BF-SHM. Furthermore, previous works with dual PZTs have been carried out on quasi-isotropic structures but, to our knowledge, no studies have been reported on anisotropic structures. In such materials, the amplitude as well as the propagation speed of A_0 and S_0 modes on a path between two PZTs depends on the angle between the path direction and the orientation of the carbon fibers composing the structure [9]. Since the mode decomposition method depends on the amplitude ratio between both modes, the PZT positions (in terms of distance and orientation) need to be chosen carefully to guarantee a sensibility of both modes in any configuration.

3

The second objective of the present work is then to propose a method to determine the optimal distance and orientation between neighbor dual-PZTs. Another underlying objective is to optimize the number of active elements which is a key point for industrial deployment specially in aeronautical applications
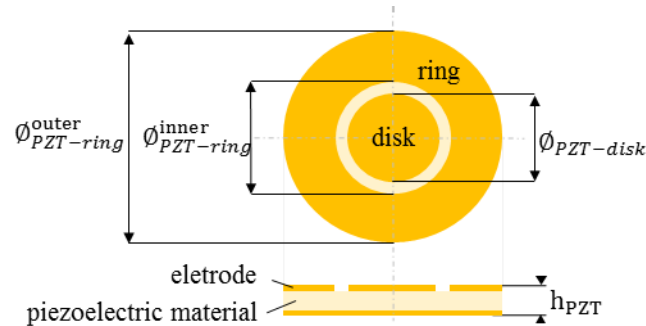

Figure 1 : Simplified view of a dual PZT composed of a concentric ring and a disk.

Some of the BF-SHM methods, where mode decomposition using dual PZT is of interest, are here quickly reviewed. The *"instantaneous baseline"* method is based on a transducer network with paths having the same dimensions and orientations. Instead of comparing signals obtained at unknown conditions with a pristine baseline, signals are compared instantaneously between paths even under varying environmental conditions [15, 21–24]. Drawbacks concern examined paths that must have identical PZT positioning and bonding and avoidance of elastic waves reflections from boundaries. Another technique called the *"time reversal"* process assumes that for a pristine structure by sending back the reverse signal received by a given PZT, the input signal used in first place should be recovered. A damage potentially breaks this relation, allowing for its detection. This method has been validated on composite structures [11, 25–28] and its limitations have been identified [29]: a high dependency on the excitation frequency, mode dispersion, and reflections from boundaries. In the *"reciprocity principle"* method, two signals obtained from both possible directions of a given path are directly compared. This method has been used successfully in aluminum [15, 19, 30] and quasi-isotropic composite [12] structures. Its drawbacks are that the implemented PZTs must be identically bonded to the structure, and that damages localized far from the investigated path are difficult to detect.
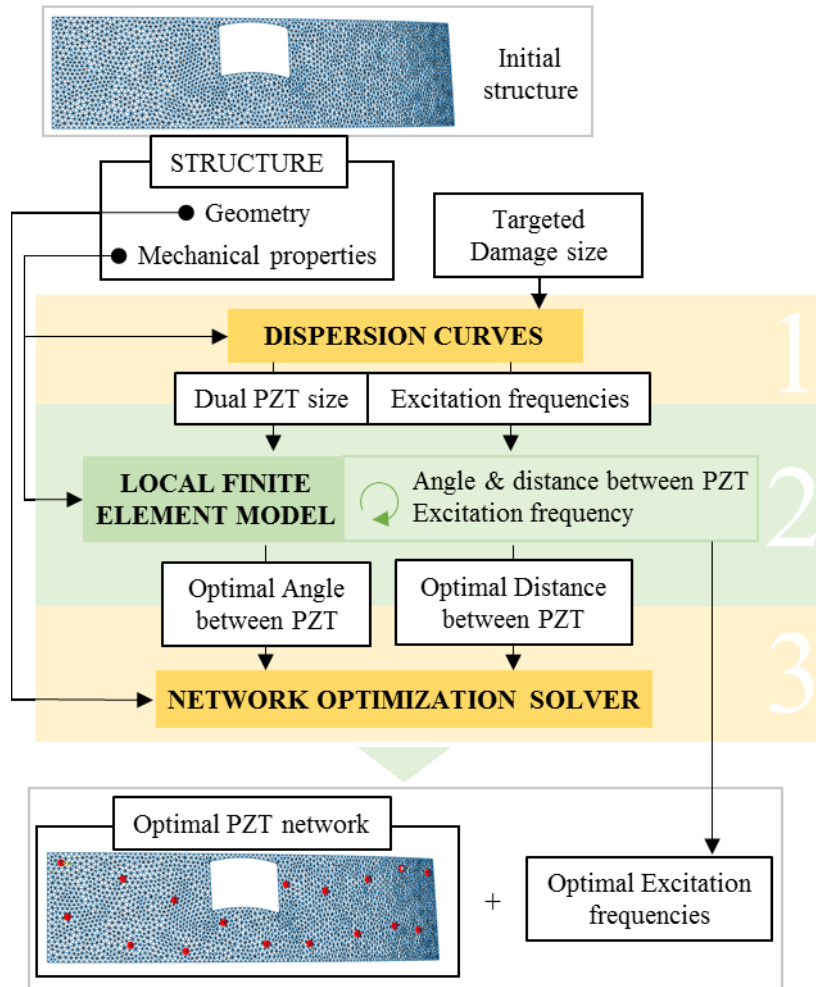
Figure 2: Different steps for the optimal design of a dual-PZT network on an anisotropic composite structure.

BF-SHM studies focus on the description of damage detection methods, but do not address the problem of network design when dealing with large structures. However, the PZT network (size, number, distance, and orientation of transducers as well as excitation frequency) to be used highly depends on the considered damage detection method, the environmental conditions, and the geometry of the structure. This step must thus be considered with great care. There have been studies on Optimal Sensor Placement (OSP) for reference-based Lamb-wave based SHM applications [31–36] with recent focus on composite structures [36–38]. These studies show that relevant criteria for PZT positioning are the distance between two neighbor PZTs and the presence of complex geometries [37] (large holes, stiffeners…) on paths between PZT. In BF-SHM applications, additional and very restrictive constraints on PZT networks exist. Based on the observations described above, the current work proposes an

original three-step process to design an optimal dual-PZT network for a structure to be monitored by means of BF-SHM methods. As depicted in figure 2, the different steps of this process are:

1. The mechanical properties of the structure are used to compute the dispersion curves of Lamb waves in the investigated material. Dispersion curves and the minimal size of the damage to be detected allow sizing dual-PZTs and determining excitation frequencies of interest.

2. A local FEM model (a plate corresponding to a small part of the monitored structure) equipped with two dual-PZTs is used. Lamb wave attenuation with distance r and orientation θ and for different excitation frequencies f_0 is extracted. Two original indexes quantifying the ability of the set (f_0, r, θ) for mode decomposition are then computed. This provides optimal parameters $(\hat{f}_0, \hat{r}, \hat{\theta})$ for neighbor dual-PZTs of the network.

3. The network optimization solver applies the optimal parameters obtained from the local FEM model to the real structure to propose a candidate optimal dual-PZT configuration.

The rest of the paper is organized as follows, in section II, the material and geometry of the targeted aeronautical structure under study are presented. Then in section III, each step of the process is described and illustrated with results obtained on a highly anisotropic composite material. Finally, in sections IV and V, PZT networks obtained for different geometries and different composite materials are displayed, analyzed and discussed.

2. Material and structure under study

Composite materials are of great interest in an aeronautical context since they provide lighter structures having the same mechanical properties than previously used materials. The composite material under study is a highly anisotropic composite fiber reinforced polymer (CFRP) with 16 plies oriented at [0°/ 90°]. Mechanical properties of one ply are listed in table 1.

Table 1: Properties of a layer of the CFRP composite laminate.

E_1 [GPa]	$E_2 = E_3$ [GPa]	ν_{31}	$\nu_{23} = \nu_{12}$	$G_{23} = G_{31}$ [GPa]	G_{12} [GPa]	ρ [kg. m^{-3}]
121	8.6	0.06	0.31	4.3	5.9	1520

A part of a nacelle from an A380 plane (the fan cowl as shown in figure 3) is considered to illustrate the three-step process proposed to design an optimal dual-PZT network for BF-SHM methods. This geometrically complex structure is 2.20 m in height for a semi circumference of 5.80 m and is made of composite monolithic carbon epoxy material. Piezoelectric elements manufactured by NOLIAC (see table 2) are used to trigger and collect Lamb waves in that structure.

Table 2: Electro-mechanical properties of the PZT material NCE51 from Noliac.

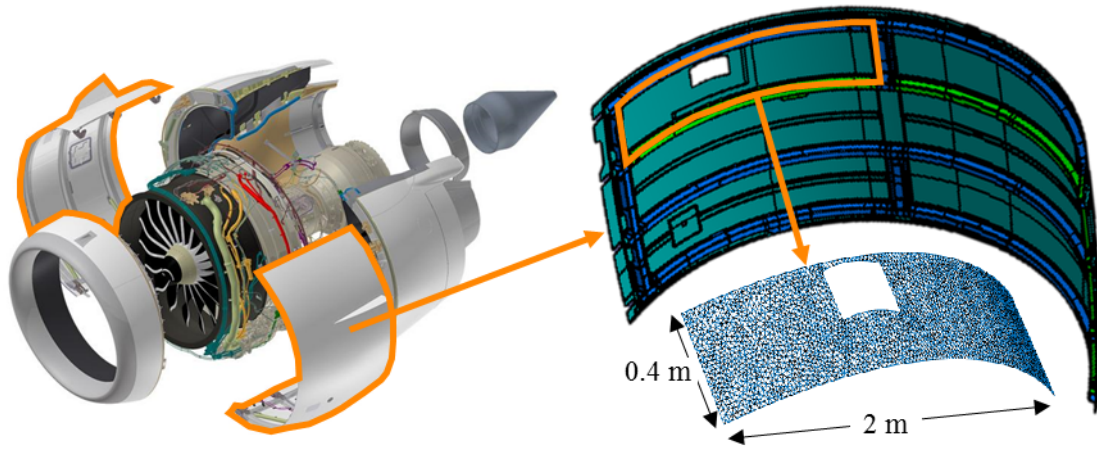| E_{11} [GPa]	E_{33} [GPa]	a [1/K]	ν	d_{31} [pC/N]	d_{33} [pC/N]	s_{11}^E $.10^{-12}$	s_{33}^E $.10^{-12}$	ρ [kg. m^{-3}]
62.50	52.63	2.10^{-6}	0.38	-195.00	460.00	16.00	19.00	7600

Figure 3: Aircraft nacelle (left), original fan cowl geometry and simplified 3D geometry of the subpart studied (right).

3. Optimal dual PZT sizing and placement

1.1 PZT dimension and excitation frequency

In this first step of the proposed method, the dimensions of the PZT to be used as actuators and sensors and the excitation frequencies are determined based on the material properties and on the minimal size of the damage to be detected. This approach is developed to meet three main goals (see figure 4):

(i)   Only the first symmetric and antisymmetric modes S_0 and A_0 must be generated,

(ii)   The dual PZT used as an actuator and the frequencies of the signal used must guarantee the excitation of S_0 and/or A_0 modes with a wavelength small enough to interact with the targeted minimal damage,

(iii)   The dual PZT used as sensor must be sensitive to both S_0 and A_0 modes on the selected range of excitation frequencies.
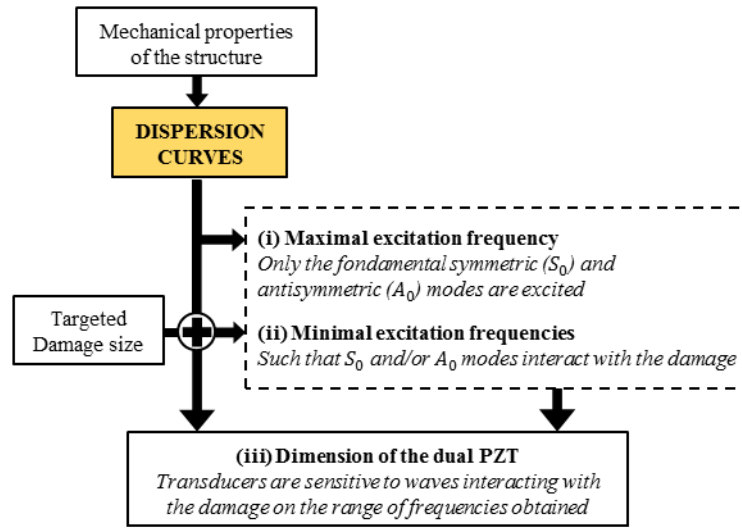

Figure 4: Schematic illustration of the three steps followed to select the dimensions of the dual PZT from dispersion curves. This corresponds to Step 1 in figure 2.

Dispersion curves are computed numerically by finding all the possible frequencies that satisfy Lamb waves dispersion relations with iterations on the wave number k [39]. Once those values are computed, the dispersion curves can be displayed as the variation of wavelength $\lambda = 2\pi/k$ of each symmetric and antisymmetric modes with frequency. Dispersion curves can also be computed for some rheological materials (please refer to [40] for an open software). The dispersion curves displayed in figure 5 are computed considering plane waves propagating in a homogenized material with the properties given in table 3 corresponding to the 0° direction of a $[0°, 90°]_{16}$ CFRP plate. The 0° orientation is chosen since it is the direction where wavelengths are larger, hence a dual PZT dimensioned for those wavelength will respect criteria described in figure 4 in all orientations.

E [GPa]	ν	ρ [kg. m^{-3}]	t [mm]
45.5	0.09	1600	2

BF-SHM methods targeted here consist in tracking S_0 and A_0 mode conversion and attenuation. It is thus necessary to restrain the domain of applications where only those first two modes propagate. Dispersion curves for higher frequencies (not displayed here) show that the excitation frequency should not exceed $f_{max} = 906$ kHz (corresponding in our case to the minimal excitation frequency for which mode A_1 is generated) to meet this condition. A second point to consider is that theoretically half the wavelength λ of the wave used to detect a damage must be shorter than or equal to the size of the damage $\emptyset_d$ in order to allow an interaction with it [41]:

$$\frac{\lambda}{2} \leq \emptyset_d \tag{1}$$

This leads us to bound the frequency range under which S_0 and A_0 can be exploited: the largest wavelength validating equation (1) is $\lambda_d = 2 \times \emptyset_d$. According to this criterion, the excitation frequency used should be greater than a frequency f_{A_0} for A_0 mode and f_{S_0} for S_0 mode, corresponding to excitation frequencies for which wavelength λ_{A_0} and λ_{S_0} are lower than λ_d. (see figure 5). As advised by the aeronautical manufacturer who provided the samples, the minimal damage size that must be detected (BVID for Barely Visible Impact Damage) is 20 mm, hence in our case, $\lambda_d = 40$ mm, $f_{A_0} = 12$ kHz and $f_{S_0} = 134$ kHz (see figure 5).

Furthermore, it is mandatory to ensure that at these frequencies the dual-PZT element can actuate and receive the desired modes. This then leads us to select optimal dual PZT dimensions. Two criteria are important in the choice of the PZT according to [42]:

- as an actuator, the optimal PZT size $\emptyset_{PZT}$ is obtained for

$$\emptyset_{PZT} = \lambda\left(n + \frac{1}{2}\right), \ n = 0,1,2,\dots \tag{2}$$

9

- as a sensor, the sensitivity of the PZT increases as its size is reduced and the size of the PZT must be inferior to half the wavelength to be detected, *i.e.*

$$\emptyset_{PZT} \leq \frac{\lambda}{2} \tag{3}$$

When classic circular PZT are used as actuators and sensors, the optimal PZT size is obtained for $\emptyset_{PZT} = \emptyset_d$ by considering criteria described by equations (1), (2) and (3). However, this choice limits in practice the application of detection to very few excitation frequencies. An advantage of the dual PZT, in addition to its mode decomposition ability, is that both parts of the PZT can be chosen independently. Nevertheless, as the disk part of the dual PZT is also used as an actuator for the mode decomposition process, it should not be too small to allow the generation of Lamb waves. The choice of ring part dimension of the dual PZT, $\emptyset_{PZT-ring}$ is chosen such that the maximum energy (see equation (2) with $\lambda = \lambda_d$ and $n = 0$) is communicated to the structure for the targeted minimal damage size. According to [42], the equivalent diameter for a ring PZT $\emptyset_{PZT-ring}$ can be determined as the outer diameter minus the inner diameter *i.e.*

$$\emptyset_{PZT-ring} = \emptyset_{PZT-ring}^{outer} - \emptyset_{PZT-ring}^{inner} = \emptyset_d \tag{4}$$

In our case, it gives $\emptyset_{PZT-ring} = 20$ mm. The choice of the central part dimension of the dual PZT $\emptyset_{PZT-disk}$ is governed by the range of frequencies on which BF-SHM methods will be investigated. In the case presented in figure 5, it is interesting to have sensors sensitive to both modes for frequencies up to f_{S_0} because it is the smallest frequency for which both modes are activated and interact with the targeted damage size. To guarantee the sensitivity of the A_0 mode at this frequency, the dimension of the central part of the dual PZT should be sensible to wavelength equal to $\lambda_{min} = \lambda_{A_0}(f_{S_0})$ (wavelength of mode A_0 obtained at f_{S_0}, see figure 5). Using equation (3), this dimension of the disk is obtained for:

$$\emptyset_{PZT-disk} = \lambda_{A_0}(f_{S_0})/2 \tag{5}$$

In the current application, $\lambda_{min} = 11$ mm, hence $\emptyset_{PZT-disk} = 5.5$ mm.
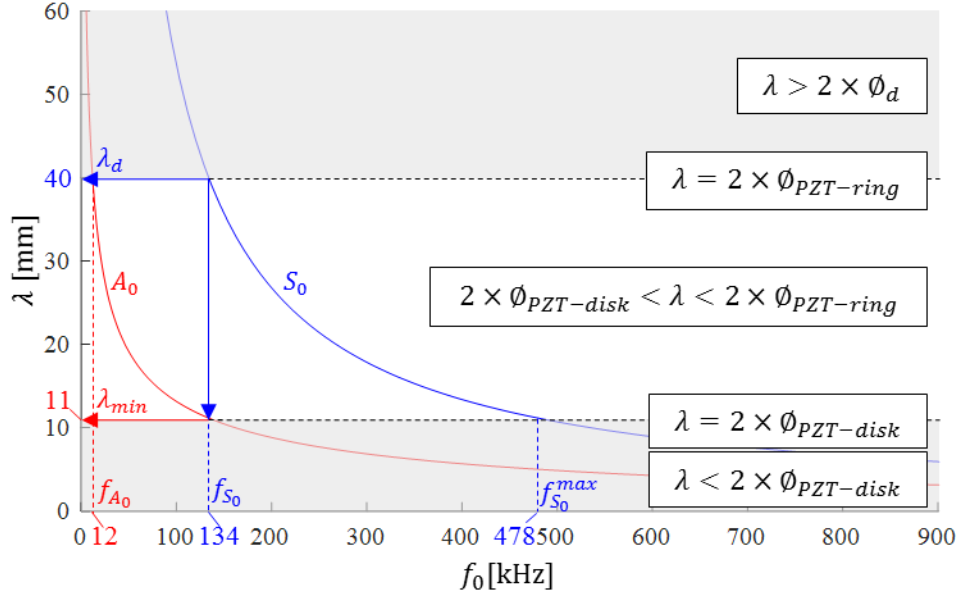
Figure 5: Dispersion curves for material described in table 3. It shows the minimum frequency to use ($f_{A_0} = $ 12 kHz for A_0 mode and f_{S_0}=134 kHz for S_0 mode) to allow for an interaction between the propagating wave and a damage of size $\emptyset_d = 20$ mm. It also shows the range of frequencies to use to guarantee a sensitivity of the dual PZT to A_0 mode and S_0 mode for frequencies up to $f_{S_0} = 134$ kHz. The disk part of the dual-PZT is also sensible to S_0 mode up to $f_{S_0}^{max} = 478$ kHz. $\emptyset_{PZT-disk} = 5.5$ mm and $\emptyset_{PZT-ring} = \emptyset_d = 20$ mm.

Figure 5 highlights four distinguishable areas:

- $0 < f_0 < f_{A_0}$: the dual PZT triggers A_0 mode but it does not interact with the damage

- $f_{A_0} < f_0 < f_{S_0}$: the dual PZT triggers A_0 and S_0 modes but only A_0 mode interacts with the damage. Both modes can be properly measured by the disk part of the dual PZT, but the ring part is theoretically only sensitive to the S_0 mode.

- $f_{S_0} < f_0 < f_{S_0}^{max}$: the dual PZT triggers A_0 and S_0 modes and both modes interact with the damage, but only S_0 mode can be properly measured by the disk part of the dual PZT, and the ring part is theoretically insensitive to any mode.

- $f_0 > f_{S_0}^{max}$: the dual PZT triggers A_0 and S_0 modes and both modes interact with the damage, but the PZT is not sensitive to any mode.

11

According to the PZT manufacturer (NOLIAC), the gap between the two electrodes designed on the upper surface of the PZT should not be less than 1 mm. Following this instruction and equations (4) and (5) the dual PZT dimension must respect:

$$\emptyset_{PZT-disk} \leq \lambda_{A_0}(f_{S_0})/2$$

$$\emptyset^{inner}_{PZT-ring} \geq \emptyset_{PZT-disk} + 2 \text{ mm}$$

$$\emptyset^{outer}_{PZT-ring} = \emptyset^{inner}_{PZT-ring} + \emptyset_d$$

The smallest dual PZT that satisfies all those recommendations is obtained for $\emptyset_{PZT-disk} = 5.5$ mm, $\emptyset^{inner}_{PZT-ring} = 7.5$ mm and $\emptyset^{outer}_{PZT-ring} = 27.5$ mm. The associated excitation frequency range of interest is from 12 to 134 kHz because it allows mode conversion tracking for both modes while guaranteeing an interaction of the propagating Lamb waves with the damage.

3.2 Optimal distance and orientation between neighbor PZTs of the network

Two important information not provided by dispersion curves are the attenuation of waves propagating within the material and the efficiency with which both Lamb wave modes are converted to electric signals by the dual-PZT. In anisotropic materials, the attenuation varies a lot with the distance and the orientation of the fibers, and symmetric and antisymmetric modes are not identically affected. This is rarely considered in the design of the PZT network whereas it is of great importance to estimate optimal relative placement of neighbor PZTs, as illustrated in figure 6. The analysis of the electromechanical efficiency of the dual-PZT will be useful to assess the mode decomposition abilities of the chosen PZT and to validate the ability of the network to be used in a BF-SHM manner.
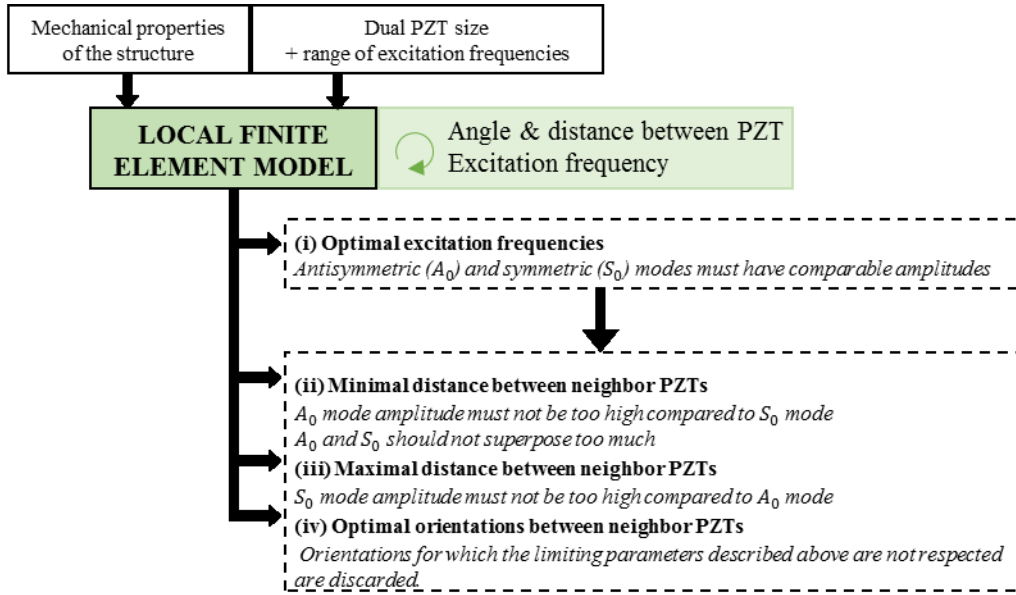
Figure 6: Schematic illustration of inputs and outputs to the local FEM (Step 2 of figure 2) as well as limiting parameters for the optimal placement of neighbor PZTs and excitation frequencies.

3.2.1   Local Finite Element Model representative of the structure

A local FEM model is built using SDTools® [43]. This model is local in the sense that it corresponds only to a FEM model of a rectangular plate made up of the same material as the whole structure instead of a FEM model of the complete structure (see figure 7 and table 2). This local approach aims at diminishing the number of nodes of the FEM model and provide an affordable simulation in terms of computation time. It is necessary in a context where parametric studies are conducted with transient simulations performed at various excitation frequencies. Quadratic elements with dimension 2 mm × 2 mm are used for the meshing of the plate. This mesh size is compatible with the wavelength of A_0 and S_0 modes which value does not exceed 11 mm on the investigated frequency range and has been validated by a convergence test. The excitation signal is chosen as a 5 cycles sinusoidal tone burst modulated by a Hanning window at an amplitude of 10 V and a central frequency f_0 varying from 10 to 140 kHz (average interval from f_{A_0} to f_{S_0} in figure 5) by steps of 10 kHz. For each step, simulations are conducted alternatively with each possible emission scheme (entire PZT, ring part, disk part), leading to a total of 30 simulations. The time step for the transient simulation is 0.36 μs and corresponds to a sampling frequency of 2.8 MHz. The transient simulation is performed with Newmark's method and

the structure dynamic damping is simulated by considering a coefficient of 5.10^{-8} for the stiffness matrix and no damping coefficient for the mass matrix (coefficients obtained from a calibration with experimental measurements and used in [44]). The plate used for the simulation is a $[0°, 90°]_{16}$ CFRP plate with the properties given in table 1 modeled as a 3D orthotropic material and homogenized using Mindlin theory for thin laminate plates. The PZT elements are composed of Noliac NCE51 material (see properties in table 2) and simulated as piezoelectric shell finite elements. The inter-distance between PZTs is 400 mm and the circle arc to study attenuation with orientation is placed 150 mm away from the actuator. Previous works, using this software, have been conducted to assess SDTools® proposed PZT elements reliability for SHM applications. Indeed, the electromechanical interaction and the effect of glue and temperature have been experimentally validated [45, 46]. The displacement is saved for each node between the actuator and the sensor to estimate Lamb wave attenuation with distance, and on the circle around the actuator to estimate Lamb wave attenuation with orientation (see figure 7).
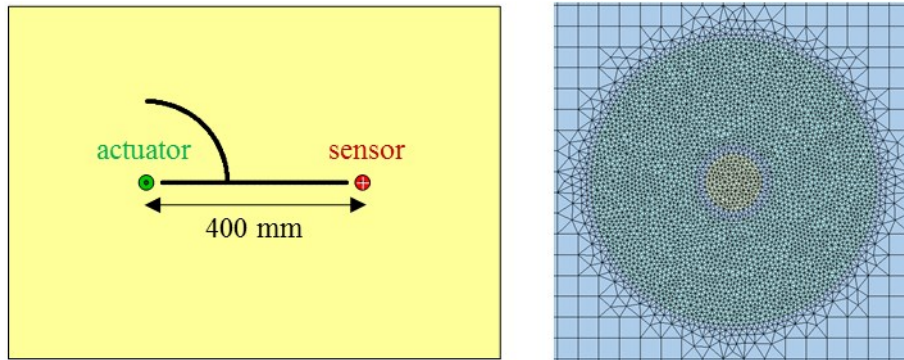

Figure 7: Local FEM composite plate with two dual PZTs and the sensing point (black line and circle) used to study antisymmetric and symmetric mode propagation (left) and mesh of the dual PZT (right)

3.2.2   Lamb waves attenuation and dual-PZT electromechanical efficiency

The electric signal measured by the dual PZT $V_{a \to s}$, depending on the PZT part used as actuator a, the PZT part used as sensor s, the distance r between actuator and sensor, the orientation compared to the 0° ply θ and the excitation frequency of the input f_0 can be analytically expressed as:

$$V_{a \to s}(r, \theta, f_0, t) = V_{a \to s}^{A_0}(r, \theta, f_0, t) + V_{a \to s}^{S_0}(r, \theta, f_0, t) \tag{6}$$

$$V_{a \to s}^{[X]_0}(r, \theta, f_0, t) = C^{[X]_0}(r, \theta, f_0, t) \times S_{a \to s}^{[X]_0}(f_0) \tag{7}$$

where t is the time, $V_{a \to s}^{A_0}$ and $V_{a \to s}^{S_0}$ refer to the electrical signal measured by the PZT for A_0 and S_0 mode when part a is used as actuator and part s is used as sensor. $[X]$ is either A or S referring to antisymmetric or symmetric mode. $C^{[X]_0}$ is independent of the actuator or sensor size as shown in [18], and corresponds to the mechanical displacement attributable to the $[X]_0$ mode at the sensor position. In the approach proposed here, the antisymmetric mode is assumed to correspond mainly to the out-of-plane deformations and the symmetric mode to correspond mainly to the in-plane deformations. $S_{a \to s}^{[X]_0}$ then corresponds to the electromechanical efficiency of the PZT to mode $[X]_0$ for actuator a and sensor s. Since $S_{a \to s}^{[X]_0}$ only depends on the excitation frequency f_0, it can be determined from the electrical signal obtained on the dual PZT electrodes of the PZT sensor and the mechanical displacements measured at the center of the sensor (the white cross in figure 7). With equations (6) and (7) and $C^{[X]_0}(r, \theta, f_0, t)$ obtained from the FEM simulation, $S_{a \to s}^{A_0}(f_0)$ and $S_{a \to s}^{S_0}(f_0)$ are computed with an iterative process that consists in finding the minimum mean square error between the envelope of the signal measured on the PZT electrode $V_{a \to s}(r, \theta, f_0, t)$ and the sum of envelopes of $C^{A_0}(r, \theta, f_0, t) \times S_{a \to s}^{A_0}(f_0)$ and $C^{S_0}(r, \theta, f_0, t) \times S_{a \to s}^{S_0}(f_0)$ (the iteration is performed on values of $S_{a \to s}^{A_0}(f_0)$ and $S_{a \to s}^{S_0}(f_0)$). Figure 10(b) shows an example of envelopes of each mode displacements scaled by their respective electromechanical efficiencies and the response signal measured by the disk part of the dual PZT.

Figure 8 shows the variation of electromechanical efficiency of ring and disk parts of the dual PZT for A_0 and S_0 mode depending on the excitation frequency. The disk part appears to be much more efficient than the ring part to measure the A_0 mode on the whole range of frequencies considered, whereas both parts are efficient to measure the S_0 mode. This graph echoes the results observed in figure 5 and the associated observations. It also explains the ability of dual-PZTs to decompose modes in the measured signal since each part of the dual PZTs exhibit different electromechanical efficiency for each mode.
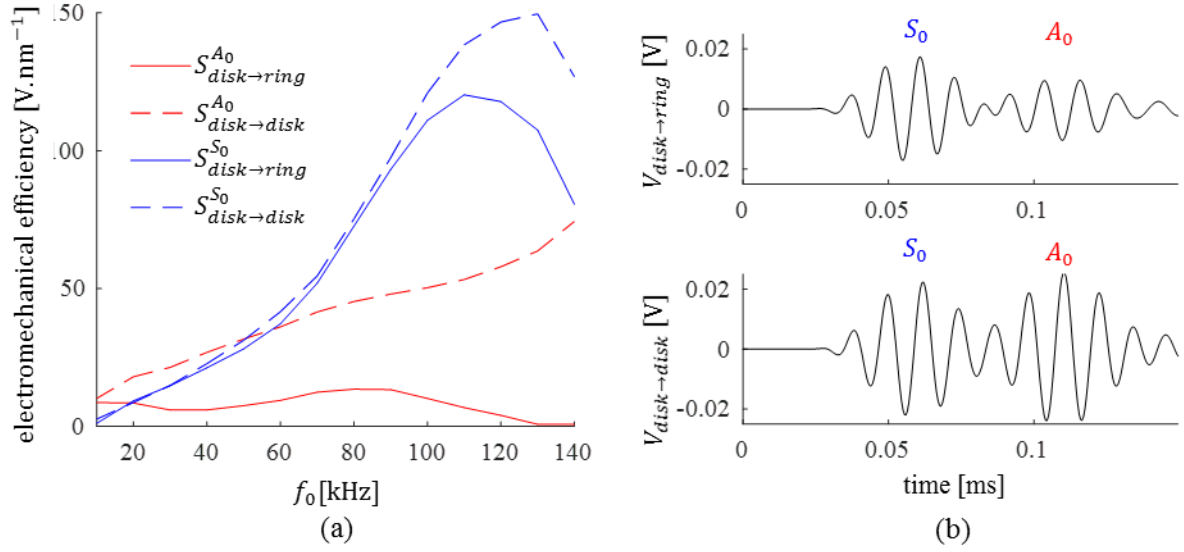
Figure 8: (a) Variation of electromechanical-efficiency of PZT sensor ring and disk for S_0 and A_0 mode against excitation frequency f_0. (b) Response signal obtained for $r = 150$ mm, $\theta = 0°$, $f_0 = 80$ kHz with the disk as actuator and the ring or the disk as sensor.

Figure 9(a) shows that A_0 and S_0 have different amplitude variation with excitation frequency: A_0 mode is significantly greater for lower frequencies (below 35 kHz) whereas S_0 mode is greater for higher frequencies (after 90 kHz). Figure 9(b) shows that A_0 mode attenuates faster than S_0 mode with distance. From figure 10(a) one can see that S_0 is much more impacted by the wave propagation direction than A_0. The S_0 mode tends to propagate well in the composite fibers directions (maximum at 0° and 90°) but its amplitude can be reduced to 10 % of its maximum value (around 17° and 73°). The A_0 mode amplitude (maximum at 0°) is only reduced to 50% of its maximum value at 45°. Figure 10 emphasizes the fact that, both modes may have the same amplitudes in the 0° direction, but this comparison varies a lot with the direction of propagation.
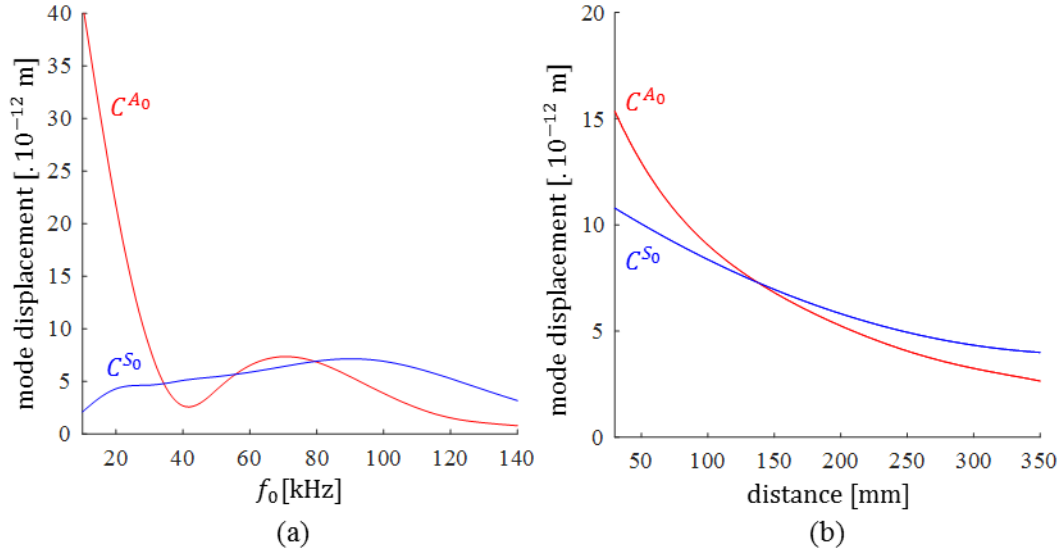
Figure 9: (a) Maximum amplitude variation of out-of-plane ($\sim A_0$) and in-plane ($\sim S_0$) displacement with frequency 150 mm away from the actuator in the 0° direction. (b) Maximum amplitude variation of out-of-plane ($\sim A_0$) and in-plane ($\sim S_0$) displacement with distance for $f_0 = 80$ kHz in the 0° direction.
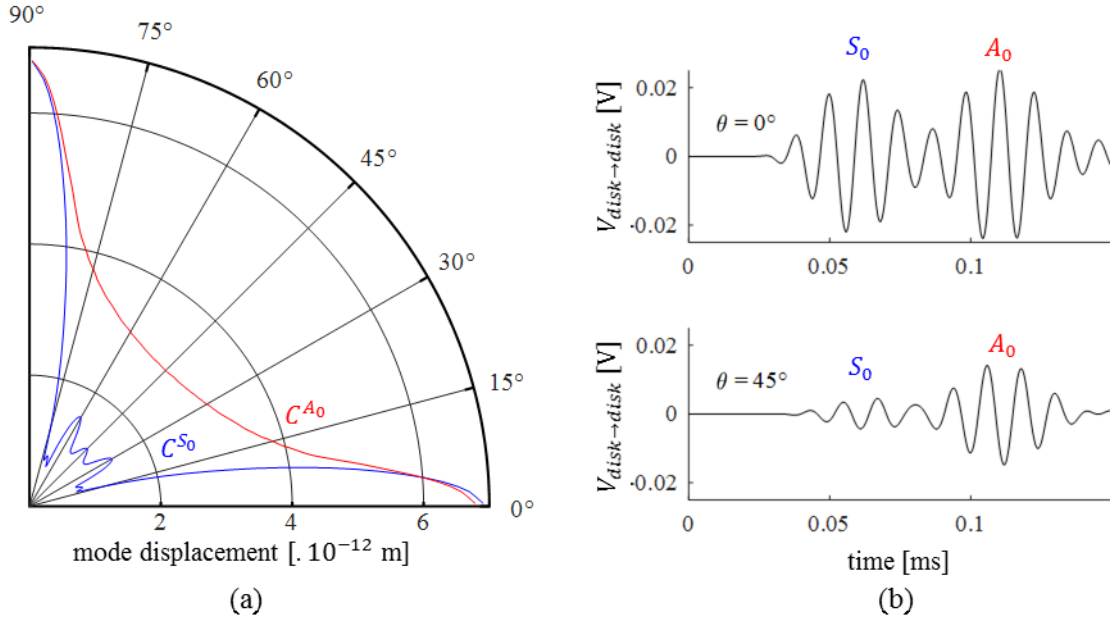

Figure 10: (a) Maximum amplitude variation of out-of-plane ($\sim A_0$) and in-plane ($\sim S_0$) displacement with orientation for $f_0 = 80$ kHz and at a distance of 150 mm from the actuator. (b) Response signal measured by the disk part of the dual PZT for $f_0 = 80$ kHz, at $r = 150$ mm and $\theta = 0°$ or $\theta = 45°$.

17

3.2.3 Optimal frequencies for mode conversion using dual PZT

In a BF-SHM context where A_0 and S_0 mode conversion and attenuation in presence of damage are investigated [10, 16, 18, 47, 48], distance between neighbors dual-PZTs and orientation of the dual PZT path with respect to fiber orientation as well as frequency of excitation must be correctly chosen such that:

    (i)   The two modes propagate and are measured in comparable proportions,

    (ii)   The first wave packet of the A_0 mode must not superpose too much with the S_0 mode.

To evaluate those two parameters, two criteria are proposed:

$$\tilde{V}_{a \to s}^{A_0/S_0}(r, \theta, f_0) = \frac{\max\left[\mathrm{env}\left(V_{a \to s}^{A_0}(r, \theta, f_0, t)\right)\right]}{\max\left[\mathrm{env}\left(V_{a \to s}^{S_0}(r, \theta, f_0, t)\right)\right]} \tag{8}$$

$$\tau_{a \to s}(r, \theta, f_0) = \frac{\int_{t_0}^{t_1} \mathrm{env}\left(V_{a \to s}^{A_0}(r, \theta, f_0, t)\right) + \int_{t_1}^{t_2} \mathrm{env}\left(V_{a \to s}^{S_0}(r, \theta, f_0, t)\right)}{\int_{t_0}^{t_3} \mathrm{env}\left(V_{a \to s}^{A_0}(r, \theta, f_0, t)\right)}, \tag{9}$$

where $\mathrm{env}(.)$ denotes the envelope of the signal. $[t_0, t_3]$ is the time interval corresponding to the first A_0 wave packet, t_1 the instant when $V_{a \to s}^{A_0}$ gets higher than $V_{a \to s}^{S_0}$, and t_2 the end of the first S_0 wave packet (see figure 12(b)). $\tilde{V}_{a \to s}^{A_0/S_0}$ represents the amplitude ratio of the contribution of the A_0 mode against the contribution of the S_0 mode in the measured response signal. $\tau_{a \to s}$ qualifies the superposition of modes in the measured response signal: it represents the intersection of both modes against A_0 mode measured in the time corresponding to the first A_0 wave packet (see figure 12(b)). These two criteria depend on the distance between actuator and sensor r, the orientation of the path actuator-sensor in comparison with the 0° ply of the structure θ, and the excitation frequency f_0. The PZT part chosen as actuator has very little influence on the criteria chosen since it affects both modes amplitudes proportionally. And as the disk part of the dual PZT is sensible to both A_0 and S_0 modes (in opposition to the ring part), only results obtained with the disk part as actuator and sensor are displayed.

We introduce two thresholds $\varepsilon_{\tilde{V}}$ and $\varepsilon_{\tilde{\tau}}$ to determine whether a sensor position and excitation frequency can be considered as suitable for mode decomposition. These thresholds will serve as tuning parameters of the proposed method. The amplitude ratio of the A_0 mode against the S_0 mode as described in equation

315

18

(8) is used to select optimal frequencies where both modes are in comparable proportion in the response measured by the disk part of the PZT. The threshold $\varepsilon_{\tilde{V}}$ is set to $1/3$ so that the amplitude of the A_0 mode should not exceed 3 times the amplitude of the S_0 mode and vice versa. Figure 11(a) shows the maximum amplitude of each mode contribution obtained with equation (7) for the disk part of the dual PZT at 150 mm from the actuator (the electromechanical efficiency of the sensor according to frequency $S_{a \to s}^{[X]_0}$ is considered). The striped area depicts the frequency range for which the amplitude ratio does not respect the threshold ($\tilde{V}_{a \to s}^{A_0/S_0} > 1/\varepsilon_{\tilde{V}}$)). Hence, the optimal frequency range to observe mode conversion is from 40 to 140 kHz. This graph also shows that the optimal frequencies for A_0 mode studied alone would be for frequencies below 40 kHz because the amplitude of the A_0 mode is significantly higher than the S_0 mode. 30 kHz corresponds to the "sweet spot frequency" of the A_0 mode in mode tuning methods. Those methods consist in an appropriate selection of the excitation frequency of Lamb waves in order to generate only one of the Lamb wave modes [13, Para. 8.8]. The frequency range obtained here is for the $0°$ orientation and is discussed for other orientations later. Figure 11(b) shows the contribution of each mode on the measured response signal. A difference between the maximum amplitude of the response signal ($V_{disk \to disk}$) on wave packets corresponding to S_0 (first wave packet) and A_0 (second wave packet) and the maximum amplitudes of each mode contribution ($V_{disk \to disk}^{A_0}$ and $V_{disk \to disk}^{S_0}$) is noticed because a little mode conversion (from S_0 to A_0) occurs at the edge of the ring part of the PZT and is measured by the disk part.
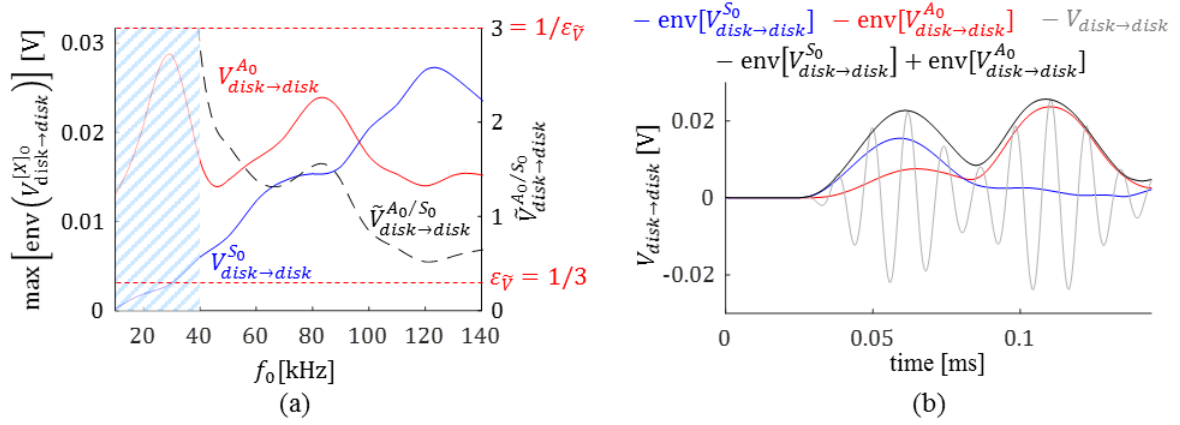
Figure 11: (a) Maximum amplitude of $V^{A_0}_{disk \to disk}$ and $V^{S_0}_{disk \to disk}$ in the response signal measured by the disk part of a dual PZT place for $r = 150$ mm. The striped area represents the frequency range where the amplitude ratio $\tilde{V}^{A_0/S_0}_{a \to s}$ (right axis) between maximum amplitude of $V^{A_0}_{disk \to disk}$ and $V^{S_0}_{disk \to disk}$ does not respect the threshold $\varepsilon_{\tilde{V}} = 1/3$. (b) Superposition of contributions of each mode and the signal measured by the disk part of the dual PZT for $f_0 = 80$ kHz, at $r = 150$ mm and $\theta = 0°$.

3.2.4 Optimal distance and orientation between neighbor dual-PZTs

The minimum distance is obtained by observing the superposition τ described in equation (9). Results displayed in figure 12(a) show that a minimum distance r_{min} of 150 mm must be respected to avoid superposition of the modes in the chosen excitation frequency range, and the superposition threshold $\varepsilon_{\tilde{\tau}}$ is set to 5% based on decomposition algorithm results observations. This allows us to clearly distinct between S_0 and A_0 modes.
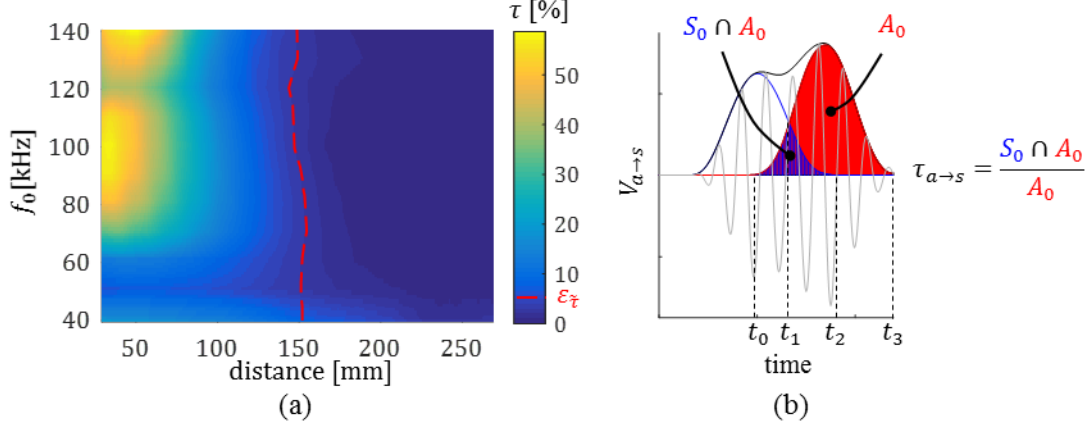
Figure 12: (a) Mode superposition against distance and excitation frequency for direct contribution of Lamb waves propagating in the 0° direction of a composite plate measured by the disk part of the dual PZT. (b) Representation of the superposition criteria estimation (equation (9)).

Given the orientation of the plies of the composite structure under study, it is relevant to notice that there is a symmetry in the wave propagation such as propagation from 0° to 45° is exactly the opposite of the propagation from 90° to 45° (this is observable on the results displayed in figure 10). First, from figure 10 (a), orientation $17°[\pi/2]$ and $73°[\pi/2]$ should be avoided since S_0 mode hardly propagates in those directions. Since A_0 and S_0 modes have different amplitude variations with frequency (see figure 9(a)), distance (see figure 9(b)), and orientation (see figure 10), the amplitude criteria $\tilde{V}_{a\to s}^{A_0/S_0}$ cannot meet the threshold $\varepsilon_{\tilde{V}}$ for every excitation frequency, orientation and distance. Figure 13 shows the amplitude ratio as measured by the disk part of the dual PZT for varying excitation frequencies and orientation. It shows that for 150 mm (minimum distance for the superposition criteria), the threshold is exceeded for excitation frequencies above 100 kHz and orientations 10° away from fiber directions. Except for an excitation frequency of 40 kHz, this observation is not applicable for 300 mm (because A_0 mode attenuates faster than S_0 mode, see figure 9(b)). However, at this distance the threshold is not respected for frequencies higher than 130 kHz. Therefore, the range of frequencies is reduced to 50 to 140 kHz, minimum distance between actuator and sensor r_{min} is evaluated at 230 mm (for shorter distance, A_0 mode is too high compared to S_0 mode at $f_0 = 60$ kHz) and maximum distance r_{max} is evaluated at 270 mm (for larger distances, S_0 mode is to high compared to A_0 mode for $f_0 = 140$ kHz and $\theta = 0°$).
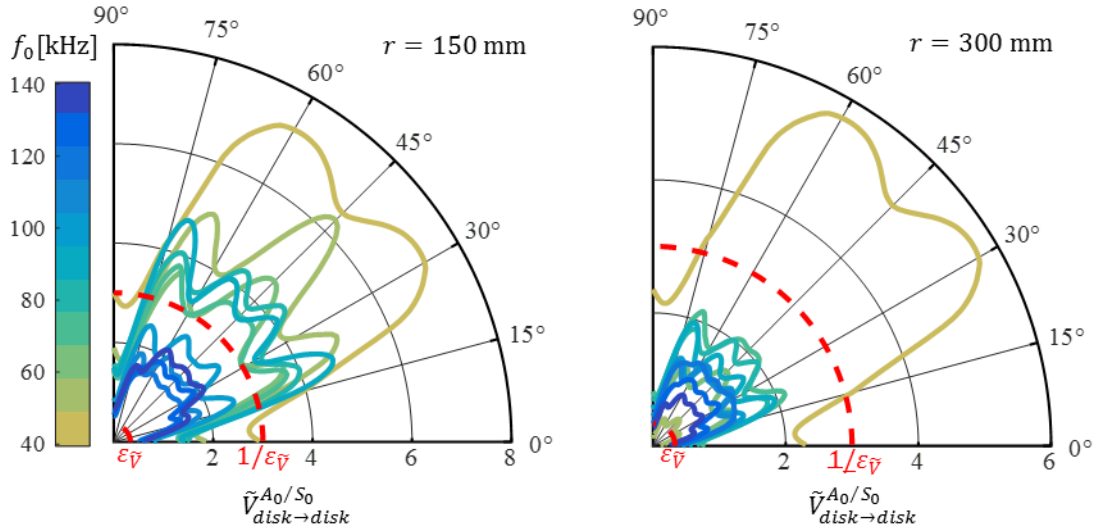
Figure 13: Amplitude ratio of the A_0 mode against S_0 mode amplitude and excitation frequency for $r = 150$ mm and $r = 300$ mm.

Figure 13 shows that the amplitude ratio at high frequencies is the limiting parameter for the maximum distance between two PZT neighbors. On the one hand, having a larger range of frequencies enables to robustify damage detection process (since damage indexes can be applied to several excitation frequencies), and on the other hand, reducing the range of frequencies toward lower accepted values lead to greater maximal distances r_{max}, which means fewer PZT on the targeted network. Hence, a tradeoff between the robustness of the detection and the number of PZT is necessary.

3.3 PZT network optimization solver

The previous simulation step allows the determination of PZT placement requirements given by the minimum and maximum distance between PZT (r_{min} and r_{max}), and optimal angles of PZT paths compared with the 0° orientation of the structure (θ_{opt}). Those requirements and the mesh of the structure under study constitute the input parameters of the PZT network optimization as described in the following algorithm:

Algorithm: PZT placement

Step 1: First PZT node is randomly selected

- A node of the mesh is randomly selected and validated as the first PZT position

End

Step 2: Other PZT nodes are chosen

- One PZT node is selected as the reference node from the nodes already validated as PZT positions.

- All the nodes respecting the requirements (eligible nodes) are determined. To be selected, a node must:

    (i) respect a distance at least equal to r_{min} from all the validated PZT positions

    (ii) respect a distance at most equal to r_{max} with the node selected as reference

    (iii) respect an orientation belonging to the optimal angles θ_{opt} with the node selected as reference.

- One node is randomly selected among nodes respecting the requirements and added to the validated PZT positions. Eligible nodes common to multiple PZT nodes and farthest node from existing PZT nodes are favored.

End

Step 3: The algorithm stops

- The distance between each node of the mesh and the validated PZT positions is computed.

- If each node of the mesh is at a distance lower than r_{max} of any PZT, the algorithm stops. Else, it returns to step 2.

End

This approach may appear basic compared to other studies focusing on network optimization but allows for a simple transition from a local model to a larger structure. A constraint on boundary conditions is also considered to avoid border reflection influence on measured signals. Figure 14 shows the solver process for the selection of the first 3 PZT nodes respecting r_{min}, r_{max} and θ_{opt}. The "forbidden"

orientation refers to orientations $17°[^\pi/_2]$ and $73°[^\pi/_2]$, corresponding to orientation not contained in

θ_{opt}. It is important to notice that the placement requirements are constrained by the capability of two

neighbor PZTs to allow mode decomposition on the path they form: if a dual PZT is placed in a

"forbidden orientation" (see figure 14), the decomposition process may be difficult to apply. However,

a damage in this zone will always interact with the propagating waves (at least with the A_0 mode since

it is less influenced by plies orientations than the S_0 mode, and is generated on all the given excitation

frequency range with wavelength allowing an interaction with the targeted damage size), hence the

influence of the damage on both modes will still be measured by the dual PZT path. In an aeronautical

context, the minimum number of transducers should be observed for weight purposes. In practice, the

algorithm considers this by taking a minimal distance which is close to r_{max} instead of r_{min}.
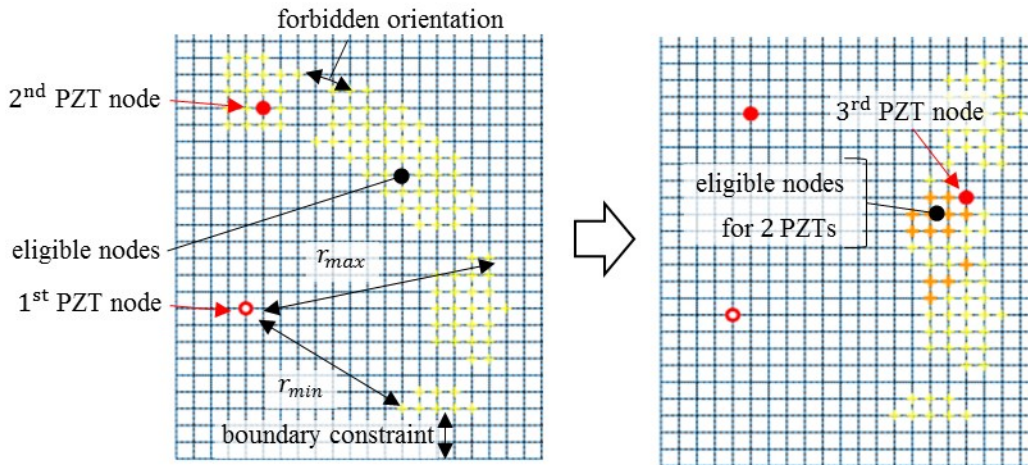

Figure 14: Illustration of the solver parameters and PZT node selection process. The optimization solver choses

nodes that are optimal for the maximum number of PZT nodes available.

4. Results

4.1 Tested cases

Four different cases (described in table 4) are considered in order to show the applicability of the

process to different structures. These cases are considered to show the influence of the anisotropy of the

material on the PZT network proposed, and the implementation to 2D and 3D structures. Two different

24

geometries and three materials are used. The first geometry - called "Plate" - is a large plate of $2000 \times 500 \times 2$ mm^3, and the second one is the geometry of the subpart from the fan cowl (see figure 3). Three different materials are compared (see table 4). The first one is the highly anisotropic CFRP with 16 plies oriented at $[0°/90°]$, used for structure #1 and #4. The second material is an isotropic material with simplified properties as displayed in table 3 used for structure #2. The third one is a quasi-isotropic CFRP with 16 plies oriented at $[0°/90°/45°/-45°]$ and properties of each ply described in table 1 (same ply properties as structure #1 and #4).

Figure 15 shows the variations of amplitude of A_0 and S_0 modes with orientation depending on the material properties.
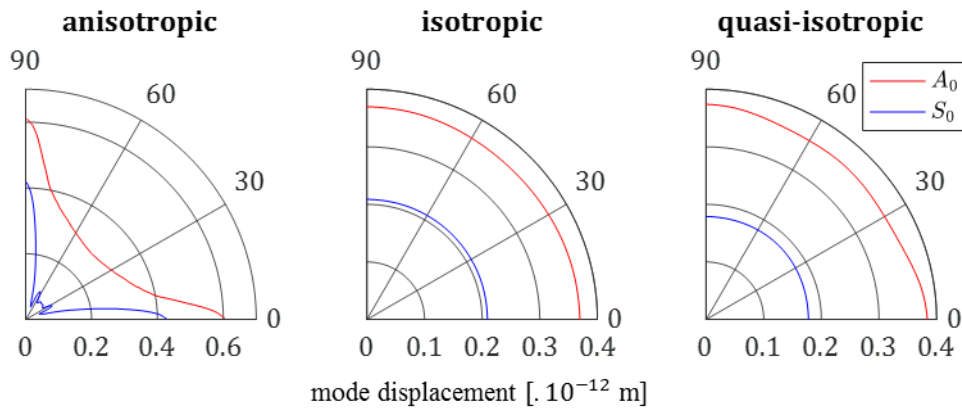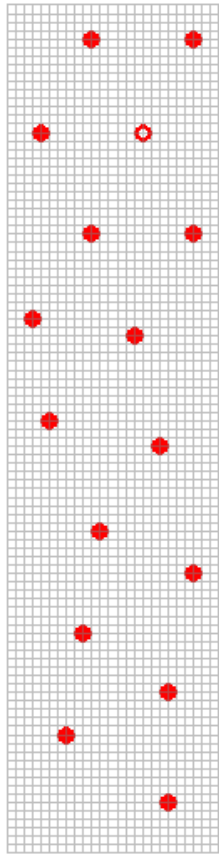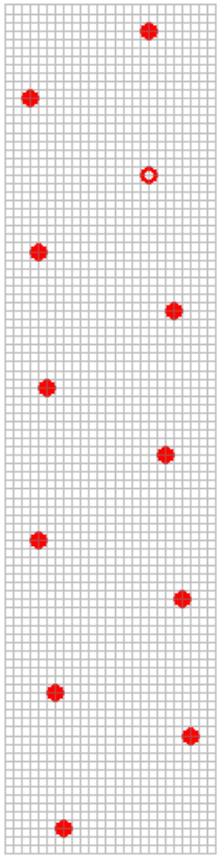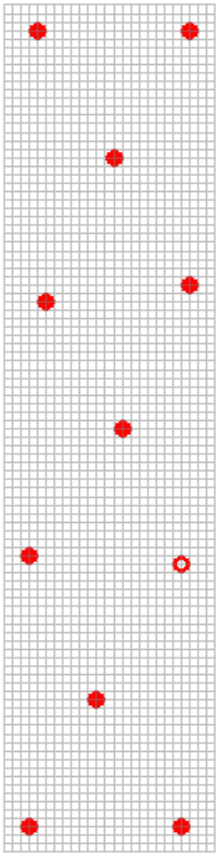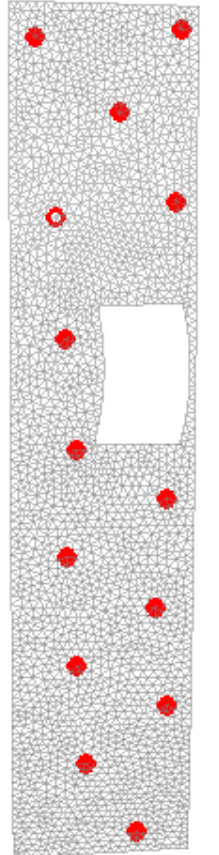

Figure 15: Mode attenuation for the three materials used in the tested cases of A_0 (red) and S_0 (blue) with varying orientation at $f_0 = 100$ kHz and a distance of 150 mm from the disk part of the dual PZT used as actuator.

4.2 Results

Table 4 sums up the results obtained for the dual PZT network implementation on the four different structures described in the previous paragraph. For each structure, outputs, from each step, are displayed.

Table 4: Application of the process on four different structures

		structure #1	structure #2	structure #3	structure #4
	Geometry	Plate	Plate	Plate	Fan Cowl
	Material	$[0°/90°]_{16}$	isotropic	$[0°/90°/45°/-45°]_{16}$	$[0°/90°]_{16}$
STEP 1 OUTPUT	$\emptyset_{PZT-disk}$ [mm]	5.5	5.5	5.5	5.5
	$\emptyset_{PZT-ring}^{inner}$ [mm]	7.5	7.5	7.5	7.5
	$\emptyset_{PZT-ring}^{outer}$ [mm]	27.5	27.5	27.5	27.5
	f_0 [kHz]	$12\cdots134$	$12\cdots134$	$13\cdots138$	$14\cdots134$
STEP 2 OUTPUT	r_{min} [mm]	230	150	150	230
	r_{max} [mm]	270	350	360	270
	$\theta_{forbidden}$ $[[\pi/2]°]$	17,73	-	-	17,73
	f_0 [kHz]	$50\cdots140$	$50\cdots140$	$50\cdots140$	$50\cdots140$
STEP 3 OUTPUT	PZT network				
	Number of PZT	16	12	11	14

4.3 Observations

For all structures, same dual PZT dimensions are advised as output of step 1 (see table 4). Actually, variations of mechanical properties of the material influence more the usable range of frequencies than the dimensions of the dual PZT. Dual PZT dimensions would be more affected by changing damage sizes (downsized as the damage size is lowered and vice-versa). For the chosen composite materials, there is very little variation of the mechanical properties, hence the range of excitation frequencies obtained with the dispersion curves do not change a lot. The frequency range would be more affected by a change in the thickness of the material: for a given material if the thickness is divided by n, the range of frequencies obtained as output of step 1 would be divided by n.

Comparing results obtained for structure #1 and #2 from table 4 shows the influence of the anisotropy of the structure on the PZT network. For the isotropic material, there is no amplitude variations of modes with orientation (see figure 15), and a greater distance between transducers r_{max} can be achieved with respect to the superposition and amplitude ratio criteria. This greater distance and the fact that there is no orientation constrains for structure #2 leads to a smaller PZT network of only 12 dual PZTs, compared to the 16 obtained on the anisotropic case of structure #1. The minimum distance ($r_{min} = 150$ mm) of structure #2 is imposed by the superposition criteria in opposition to #1 where minimum distance ($r_{min} = 230$ mm) is imposed by the amplitude ratio criteria.

Structure #2 and #3 show very little difference since mode attenuation with orientation for those two materials is very similar, and in both cases, S_0 and A_0 modes amplitude is constant with orientation contrary to the anisotropic material (see figure 15). S_0 mode amplitude in the isotropic case is greater than in the quasi-isotropic case leading to a smaller maximum distance between transducers ($r_{max} = 350$ mm for structure #2 and $r_{max} = 360$ mm for structure #3).

Comparison of results obtained for structure #1 and #4 from table 4 shows the ability of the algorithm to be applied on 3D meshes and to provide a PZT network that respects the placement constraints. The introduction of a cavity in the structure is not really taken into account by the algorithm. It is somehow considered since no PZT node can be placed in the hole (it does not contain any node), the supplementary

constraint on boundary conditions is applied to hole edges, and the computing of distances between nodes takes the hole into account.

5. Discussion

The proposed method opens several discussion points:

- The sizing method described in the first step of the process is theoretical. Experimental measurements often give exploitable results even if the PZT dimensions do not respect the Lamb wave constraints. However, this theoretical approach is the first attempt to justify the dual PZT electrodes sizes, and those dimensions are consistent with physical properties of the structure and lamb wave propagation. There is not only one good sizing, but this method gives landmarks for the choice of the dual PZT, which is hardly discussed in other studies. The range of frequencies chosen does not take into account the continuous mode conversion well described in [9, Pt. IV]. However, by targeting a minimal damage size $\emptyset_d > 7$ mm (maximum width of roving in twill fabric composites), wavelengths of both modes obtained on the selected range of frequencies are larger than the eventual roving thus limiting continuous mode conversion due to coupling elements. This phenomenon could be responsible for A_0 mode measurements arriving before the main wave packet in experimental conditions.

- The thresholds for the superposition criteria and the amplitude ratio criteria may appear arbitrary but they have been empirically verified. They could be softened if the aim is to place fewer transducers on the structure or hardened if the aim is to obtain the best mode decomposition results. This article presents here a concept methodology and some parameters can be flexible.

- The large structure presented in this article is not very complex compared to other SHM applications (only one hole, no stiffener) and the proposed optimization solver would not be very robust for very complex structures. Still, the local FEM approach could be improved by integrating stiffeners, holes, and/or complex local geometries preventing the simulation from modeling the full-scale model at once.

- Hypotheses done on the local FEM are not very strong and allow to have a good appreciation of the limiting criteria for the current BF-SHM methods. Even if the model has been calibrated properly to fit the real material, future works on composite structure will allow the validation of the obtained optimal parameters meeting the targeted expectations.

- Results obtained for different structures in part 4 show that a quasi-isotropic structure behaves quite similarly to an isotropic structure concerning mode attenuation with orientation. This observation shows that for such a poorly anisotropic structure, the orientation between transducers has no influence on the designed PZT network, and larger distances can be considered since the amplitude ratio between A_0 and S_0 modes is nearly constant in all directions. In the case of the highly anisotropic structure, the amplitude of both modes highly depends on the propagation orientation, and it has a great impact on the distance and orientation between transducers.

6. Conclusion

This article presents a process to design a PZT network on a large structure for BF-SHM methods based on the tracking of mode variations in a composite structure. This work falls within the framework of research which tries to bridge the gap between laboratory research and industrial deployment of SHM processes [49]. Indeed, the method proposed in this work tackles one of the problems that hinders the deployment of a promising dual PZT BF-SHM method, which is how to choose optimally the PZT elements in terms of size, number and placements.

The first contribution of this work, is to propose a generic solution to the choice of dimensions of the dual PZT (used to decompose A_0 and S_0 mode contributions in the response signal) based on the dispersion curves and the damage size to detect. This also brings out the range of excitation frequencies that favor an interaction with the eventual damage.

The second contribution resides in the precise and careful exploitation of Lamb wave mode propagation simulated in a local FEM. Particularly, two criteria are proposed (mode superposition ratio and mode amplitude ratio) in order to define the best actuator-sensor placement (optimal distance and orientation)

and optimal excitation frequencies in a context where both A_0 and S_0 modes have to propagate in the structure and be measured by the PZT sensor. This local model gives the relevant parameters for the last key point of this article, which is a simple PZT network optimization solver. This solver guarantees that dual PZT are optimally placed on the monitored structure, and together with the local FEM avoid the need for a large-scale FEM simulation.

This article does not give an absolute method for a PZT network design but proposes a generic process: given the material and geometry of a structure, dual PZT size, placement and excitation frequencies are proposed in order to optimize the implementation of BF-SHM method on the structure to monitor. The authors have chosen to apply it on four different structures. This emphasizes the need for a local FEM for highly anisotropic structures to understand the Lamb wave propagation in such materials before being confronted with unexplainable results in real experimentation.

References

[1] K. Worden, C. R. Farrar, G. Manson, and G. Park, "The fundamental axioms of structural health monitoring," *Proc. R. Soc. Math. Phys. Eng. Sci.*, vol. 463, no. 2082, pp. 1639–1664, Jun. 2007.

[2] J. E. Michaels and T. E. Michaels, "Detection of structural damage from the local temporal coherence of diffuse ultrasonic signals," *IEEE Trans. Ultrason. Ferroelectr. Freq. Control*, vol. 52, no. 10, pp. 1769–1782, Oct. 2005.

[3] S. Roy, K. Lonkar, V. Janapati, and F.-K. Chang, "A novel physics-based temperature compensation model for structural health monitoring using ultrasonic guided waves," *Struct. Health Monit.*, vol. 13, no. 3, pp. 321–342, 2014.

[4] Y. Wang, L. Gao, S. Yuan, L. Qiu, and X. Qing, "An adaptive filter-based temperature compensation technique for structural health monitoring," *J. Intell. Mater. Syst. Struct.*, vol. 25, no. 17, pp. 2187–2198, Nov. 2014.

[5] Y. Wang, L. Qiu, L. Gao, S. Yuan, and X. Qing, "A new temperature compensation method for guided wave-based structural health monitoring," 2013, p. 86950H.

[6] G. Konstantinidis, B. W. Drinkwater, and P. D. Wilcox, "The temperature stability of guided wave structural health monitoring systems," *Smart Mater. Struct.*, vol. 15, no. 4, pp. 967–976, Aug. 2006.

[7] Y. Lu and J. E. Michaels, "A methodology for structural health monitoring with diffuse ultrasonic waves in the presence of temperature variations," *Ultrasonics*, vol. 43, no. 9, pp. 717–731, Oct. 2005.

[8] Z. Su and L. Ye, *Identification of damage using Lamb waves: from fundamentals to applications*. Berlin: Springer-Verlag, 2009.

[9] R. Lammering, U. Gabbert, M. Sinapius, T. Schuster, and P. Wierach, Eds., *Lamb-Wave Based Structural Health Monitoring in Polymer Composites*. Cham: Springer International Publishing, 2018.

[10] C. M. Yeum, H. Sohn, and J. B. Ihn, "Delamination detection in a composite plate using a dual piezoelectric transducer network," 2011, p. 798406.

[11] R. Gangadharan, C. R. L. Murthy, S. Gopalakrishnan, and M. R. Bhat, "Time reversal health monitoring of composite plates using Lamb waves," *Int. J. Aerosp. Innov.*, vol. 3, no. 3, pp. 131–142, 2011.

[12] L. Huang, L. Zeng, and J. Lin, "Baseline-free damage detection in composite plates based on the reciprocity principle," *Smart Mater. Struct.*, vol. 27, no. 1, p. 015026, Jan. 2018.

[13] V. Giurgiutiu, *Structural health monitoring with piezoelectric wafer active sensors*. Amsterdam: Academic Press/Elsevier, 2008.

[14] H. Sohn, H. J. Lim, C. M. Yeum, and J.-B. Ihn, *Reference free inconsistency detection system*. Google Patents, 2015.

[15] Y.-K. An and H. Sohn, "Instantaneous crack detection under varying temperature and static loading conditions," *Struct. Control Health Monit.*, vol. 17, no. 7, pp. 730–741, Nov. 2010.

[16] C. M. Yeum, H. Sohn, J. B. Ihn, and H. J. Lim, "Instantaneous delamination detection in a composite plate using a dual piezoelectric transducer network," *Compos. Struct.*, vol. 94, no. 12, pp. 3490–3499, Dec. 2012.

[17] C. M. Yeum, H. Sohn, H. J. Lim, and J. B. Ihn, "Reference-free delamination detection using Lamb waves" *Struct. Control Health Monit.*, p. n/a-n/a, Aug. 2013.

[18] C. M. Yeum, H. Sohn, and J. B. Ihn, "Lamb wave mode decomposition using concentric ring and circular piezoelectric transducers," *Wave Motion*, vol. 48, no. 4, pp. 358–370, Jun. 2011.

[19] H. Sohn and S. B. Kim, "Development of dual PZT transducers for reference-free crack detection in thin plate structures," *IEEE Trans. Ultrason. Ferroelectr. Freq. Control*, vol. 57, no. 1, pp. 229–240, Jan. 2010.

[20] H. J. Lim, H. Sohn, C. M. Yeum, and J. M. Kim, "Reference-free damage detection, localization, and quantification in composites," *J. Acoust. Soc. Am.*, vol. 133, no. 6, pp. 3838–3845, Jun. 2013.

[21] S. R. Anton, A. Butland, M. Carrión, M. Buechler, and G. Park, "Instantaneous Structural Damage Identification Using Piezoelectric-Based Lamb Wave Propagation," *Proc. IMAC-XXV Febr.*, pp. 19–22, 2007.

[22] S. R. Anton, D. J. Inman, and G. Park, "Reference-Free Damage Detection Using Instantaneous Baseline Measurements," *AIAA J.*, vol. 47, no. 8, pp. 1952–1964, Aug. 2009.

[23] B. Alem, A. Abedian, and K. Nasrollahi-Nasab, "Reference-Free Damage Identification in Plate-Like Structures Using Lamb-Wave Propagation with Embedded Piezoelectric Sensors," *J. Aerosp. Eng.*, p. 04016062, Jul. 2016.

[24] A. Bagheri, K. Li, and P. Rizzo, "Reference-free damage detection by means of wavelet transform and empirical mode decomposition applied to Lamb waves," *J. Intell. Mater. Syst. Struct.*, vol. 24, no. 2, pp. 194–208, Jan. 2013.

[25] H. Sohn, H. Woo Park, K. Law, and C. R. Farrar, "Combination of a Time Reversal Process and a Consecutive Outlier Analysis for Baseline-free Damage Diagnosis," *J. Intell. Mater. Syst. Struct.*, Dec. 2006.

[26] Sohn, "Damage Detection in Composite Plates by Using an Enhanced Time Reversal Method." 2007.

[27] H. W. Park, H. Sohn, K. H. Law, and C. R. Farrar, "Time reversal active sensing for health monitoring of a composite plate," *J. Sound Vib.*, vol. 302, no. 1–2, pp. 50–66, Apr. 2007.

[28] Z. Liu, X. Zhong, T. Dong, C. He, and B. Wu, "Delamination detection in composite plates by synthesizing time-reversed Lamb waves and a modified damage imaging algorithm based on RAPID," *Struct. Control Health Monit.*, p. n/a-n/a, Jan. 2016.

[29] H. W. Park, S. B. Kim, and H. Sohn, "Understanding a time reversal process in Lamb wave propagation," *Wave Motion*, vol. 46, no. 7, pp. 451–467, Nov. 2009.

[30] S. B. Kim and H. Sohn, "Instantaneous crack detection using dual PZT transducers," 2008, p. 693509.

[31] K. Worden and A. P. Burrows, "Optimal sensor placement for fault detection," *Eng. Struct.*, vol. 23, no. 8, pp. 885–901, Aug. 2001.

[32] K. Dogancay and H. Hmam, "On optimal sensor placement for time-difference-of-arrival localization utilizing uncertainty minimization," in *Signal Processing Conference, 2009 17th European*, 2009, pp. 1136–1140.

[33] H. Gao and J. L. Rose, "Ultrasonic Sensor Placement Optimization in Structural Health Monitoring Using Evolutionary Strategy," *AIP Conf. Proc.*, vol. 820, no. 1, pp. 1687–1693, Mar. 2006.

[34] Eric B. Flynn and Michael D. Todd, "Optimal Placement of Piezoelectric Actuators and Sensors for Detecting Damage in Plate Structures," *J. Intell. Mater. Syst. Struct.*, vol. 21, no. 3, pp. 265–274, Feb. 2010.

[35] E. B. Flynn and M. D. Todd, "A Bayesian approach to optimal sensor placement for structural health monitoring with application to active sensing," *Mech. Syst. Signal Process.*, vol. 24, no. 4, pp. 891–903, May 2010.

[36] C. Fendzi, J. Morel, M. Rébillat, M. Guskov, N. Mechbal, and G. Coffignal, "Optimal Sensors Placement to Enhance Damage Detection in Composite Plates," in *7th European Workshop on Structural Health Monitoring*, 2014, pp. 1–8.

[37] M. Thiene, Z. S. Khodaei, and M. H. Aliabadi, "Optimal sensor placement for maximum area coverage (MAC) for damage localization in composite structures," *Smart Mater. Struct.*, vol. 25, no. 9, p. 095037, Sep. 2016.

[38] M. S. Salmanpour, Z. Sharif Khodaei, and M. H. Aliabadi, "Transducer placement optimisation scheme for a delay and sum damage detection algorithm," *Struct. Control Health Monit.*, vol. 24, no. 4, p. n/a-n/a, Apr. 2017.

[39] H. Lamb, "On waves in elastic plates," 1917.

[40] A. Marzani and P. Bocchini, "www.guiguw.com," *GUIGUW - Guided Waves made easy*. [Online]. Available: http://www.guiguw.com/. [Accessed: 08-Jun-2018].

[41] J. L. Rose, *Ultrasonic Waves in Solid Media*. Cambridge University Press, 2004.

[42] A. Raghavan and C. E. S. Cesnik, "Finite-dimensional piezoelectric transducer modeling for guided wave based structural health monitoring," *Smart Mater. Struct.*, vol. 14, no. 6, pp. 1448–1461, Dec. 2005.

[43] E. Balmes, J. Bianchi, and J. Leclere, "Structural Dynamics Toolbox 6.2 (for use with MATLAB), SDTools, Paris, France.," 2009. [Online]. Available: http://www.sdtools.com/. [Accessed: 12-Dec-2017].

[44] M. Gresil and V. Giurgiutiu, "Prediction of attenuated guided waves propagation in carbon fiber composites using Rayleigh damping model," *J. Intell. Mater. Syst. Struct.*, vol. 26, no. 16, pp. 2151–2169, Nov. 2015.

[45] E. Balmès, M. Guskov, and J.-P. Bianchi, "Validation and verification of FE models of piezo based SHM systems," in *ISMA International Conference on Noise and Vibration Engineering*, Leuven, Belgium, 2016, p. ID 807.

[46] C. Fendzi, M. Rébillat, N. Mechbal, M. Guskov, and G. Coffignal, "A data-driven temperature compensation approach for Structural Health Monitoring using Lamb waves," *Struct. Health Monit. Int. J.*, vol. 15, no. 5, pp. 525–540, Sep. 2016.

[47] Z. Su and L. Ye, "Selective generation of Lamb wave modes and their propagation characteristics in defective composite laminates," *Proc. Inst. Mech. Eng. Part J. Mater. Des. Appl.*, vol. 218, no. 2, pp. 95–110, Apr. 2004.

[48] Y.-H. Kim, D.-H. Kim, J.-H. Han, and C.-G. Kim, "Damage assessment in layered composites using spectral analysis and Lamb wave," *Compos. Part B Eng.*, vol. 38, no. 7–8, pp. 800–809, Oct. 2007.

[49] P. Cawley, "Structural health monitoring: Closing the gap between research and industrial deployment," *Struct. Health Monit. Int. J.*, p. 147592171775004, Jan. 2018.